Photonic Weyl phase transition in dynamically modulated brick-wall waveguide arrays

CHENGZHI QIN,[1] QINGJIE LIU,[1] BING WANG,[1,*] AND PEIXIANG LU[1,2,3]

[1]*Wuhan National Laboratory for Optoelectronics and School of Physics, Huazhong University of Science and Technology, Wuhan 430074, China*
[2]*Laboratory for Optical Information Technology, Wuhan Institute of Technology, Wuhan 430205, China*
[3]*lupeixiang@hust.edu.cn*
*wangbing@hust.edu.cn

Abstract: We investigate the topological phase transition between Type-I and Type-II Weyl points (WPs) in a composite three-dimensional lattice composed of a two-dimensional brick-wall waveguide array and a synthetic frequency dimension created by dynamic modulation. By imposing different modulation amplitudes and phases in the two sublattices, we can break either parity or time-reversal symmetry and realize the phase transition between Type-I and Type-II WPs. As the array is truncated to have two edges, two Fermi-arc surface states will emerge, which propagate in opposite directions for Type-I WPs while in same directions for Type-II WPs, accompanied by bidirectional and unidirectional frequency shifts for the optical modes. Particularly at the phase transition point, we find that one of two bands becomes flat with a vanished group velocity along frequency axis in the vicinity of WPs. The study paves a way towards realizing different topological phases in the same photonic structure, which offers new opportunities to control wave transportation both in spatial and frequency domains.

1. Introduction

Weyl semimetals, hosting Weyl points (WPs) in the band structure, have emerged as new frontiers in condensed-matter physics due to the experimental discoveries in TaAs class of materials [1–6]. Weyl point is a degeneracy node between two bands in the three-dimensional (3D) momentum space near which the band structure is linear in all directions. WPs manifest chiral properties since they can act as "source" or "sink" of Berry flux that carries opposite topological charges. Accordingly, for a truncated material, there will emerge surface states in the form of Fermi arcs connecting WPs of opposite charges. Basically, there exist two types of WPs: Type-I WPs have a standard cone-like energy spectrum with a point-like Fermi surface and Type-II WPs possess a tilted spectrum with two bands touching at the contact of electron and hole pockets [7]. It is important to distinguish between these two types of WPs since they manifest different transport dynamics for the Fermi-arc surface states and distinct chiral anomaly effects in response to external electromagnetic field [8–12]. However, the type of WPs is usually fixed for a chosen Weyl semimetal material due to the difficulty in varying the lattice structures in electronic systems. Recent studies on WPs have been extend from electronic to photonic and acoustic systems [13–21]. Typically in photonic systems, the electron and hole pockets can be mimicked with diatomic lattice structures exhibiting two Bloch bands, which provides a tunable platform to explore photonic WPs. Specifically, the phase transition between two types of WPs can be realized by introducing anisotropic couplings in waveguide lattices [22] or by inducing lattice strain [23]. However, both of the above methods rely on the dramatic change or deformation of lattice structure. A question naturally arises whether we can create two types of WPs in the same lattice structure and realize the phase transition between them without changing lattice geometric structure.

Though WPs are 3D objects, it has been recently recognized that synthetic dimension can be introduced to construct WPs in the lower-dimensional physical structures [24–26]. In particular, by adding a synthetic frequency dimension through dynamic modulation, WPs can

be created in a two-dimensional (2D) resonator array arranged in the honeycomb lattice [24,25]. Moreover, WPs have been also realized in a one-dimensional photonic crystal by adopting two synthetic parametric dimensions [26]. Compared to the WPs created in truly 3D lattice structures, the synthetic dimension can simplify the system complexity of WPs and enable the flexible tunability of coupling properties. In this regard, one may ask whether it can also induce phase transition between two types of WPs.

In this work, we demonstrate that the introduction of synthetic dimension can realize the phase transition between two types of WPs based on the same photonic lattice. We propose a 2D waveguide array arranged in brick-wall lattice and create a synthetic frequency dimension by dynamically modulating the waveguide refractive indices. Brick-wall lattice represents a special case of the honeycomb lattice [27–30], both of which can be strained into each other through continuous deformation. The brick-wall lattice can support two Dirac points in the 2D Brillouin zone that can be generalized to WPs by adding a synthetic frequency dimension. By imposing different modulation amplitudes and phases in two sublattices, we can break both parity and time-reversal (T) symmetries and achieve the phase transition between two types of WPs. By truncating the brick-wall array to manifest two edges, we can obtain the Fermi-arc surface states. The two surface states of Type-I WPs propagate in the same directions while they propagate with opposite directions for Type-II WPs. Accordingly, the optical modes will experience bidirectional and unidirectional spectral shifts, respectively. In particular at the phase transition point, one of two Fermi-arc surface states will become localized with the group velocity being vanished in the frequency dimension. Finally, we show that the brick-wall lattice can be realized by inserting metallic slab between the dielectric square lattice waveguide arrays.

2. Type-I and Type-II Weyl points in a synthetic 3D lattice

We start by considering the structure of dynamically modulated brick-wall waveguide arrays. As shown in Fig. 1(a), the array consists of two types of interpenetrating waveguides A and B arranged in a square lattice. Differing from the conventional square lattice in which each site A (or B) can couple to the nearest-neighbor four B (or A) sites, one of the four coupling bonds is removed to form the brick-wall array (the dashed green arrow), leaving only three couplings bonds (solid green arrows) for each A (or B) waveguide. The blocking of coupling can be realized by inserting a metallic slab between the dielectric waveguides (not shown here), which will be discussed in detail in Sec 4. Additionally, both waveguides A and B are subject to the travelling-wave index modulations

$$n_{1(2)}(z,t) = n_0 + \Delta n_{1(2)} \cos[\Omega t - qz + \phi_{1(2)}], \tag{1}$$

where n_0 is the background refractive index, Ω and q denote the modulation frequency and wavenumber. $\Delta n_{1(2)}$, $\phi_{1(2)}$ are the modulation amplitude and initial phase in waveguides A and B, respectively. The modulation can induce photonic transitions in each waveguide and create a synthetic frequency lattice with lattice constant Ω [31–37]. The frequency lattice, combined with the 2D brick-wall lattice, constitutes a synthetic 3D lattice structure. The equivalent lattice model is shown in Fig. 1(b), with the Hamiltonian given by

$$
\begin{aligned}
H = & \sum_{i,n} \left(J_x a^\dagger_{\mathbf{r}_i,n} b_{\mathbf{r}_i+\bar{\mathbf{e}}_1,n} + J_x a^\dagger_{\mathbf{r}_i,n} b_{\mathbf{r}_i+\bar{\mathbf{e}}_2,n} + J_y a^\dagger_{\mathbf{r}_i,n} b_{\mathbf{r}_i+\bar{\mathbf{e}}_3,n} + h.c. \right) \\
& + \sum_{i,n} \left(J_{\omega 1} e^{-i\phi_1} a^\dagger_{\mathbf{r}_i,n} a_{\mathbf{r}_i,n+1} + h.c. \right) + \sum_{j,n} \left(J_{\omega 2} e^{-i\phi_2} b^\dagger_{\mathbf{r}_j,n} b_{\mathbf{r}_j,n+1} + h.c. \right),
\end{aligned}
\tag{2}
$$

where $a^\dagger_{\bar{\mathbf{r}}_i,n}(a_{\bar{\mathbf{r}}_i,n}), b^\dagger_{\bar{\mathbf{r}}_j,n}(b_{\bar{\mathbf{r}}_j,n})$ are creation (annihilation) operators for the optical mode in the waveguide A and B at frequency $\omega = \omega_0 + n\Omega$. $n = 0, \pm 1, \pm 2\dots$ is site index in the frequency lattice. $\boldsymbol{e}_1 = (a, 0)$, $\boldsymbol{e}_2 = (-a, 0)$, $\boldsymbol{e}_3 = (0, -a)$ with a being the in-plane lattice constant. The in-

plane coupling coefficients J_x and J_y are real numbers and the frequency-dimension coupling coefficients are complex ones with amplitudes $J_{\omega 1}$, $J_{\omega 2}$ and phases $\pm \phi_1$ ($\pm \phi_2$) in waveguides A and B. Note that the coupling phase $\pm \phi_1$ ($\pm \phi_2$) is equal and opposite to the modulation phase in the upward and downward frequency transitions, which can be configured to break the time-reversal symmetry. In terms of Fourier analysis, the Hamiltonian is $H = \sum_k (a_k^\dagger\ b_k^\dagger) H(k)(a_k\ b_k)^T$, with the k-space Hamiltonian given by

$$H(\mathbf{k}) = [2J_x \cos(k_x a) + J_y \cos(k_y a)]\sigma_x + J_y \sin(k_y a)\sigma_y$$
$$+ [J_{\omega 1} \cos(k_\omega \Omega) - J_{\omega 2} \cos(k_\omega \Omega - \Delta\phi)]\sigma_z \qquad (3)$$
$$+ [J_{\omega 1} \cos(k_\omega \Omega) + J_{\omega 2} \cos(k_\omega \Omega - \Delta\phi)]\sigma_0,$$

where σ_0 is the 2×2 unit matrix and σ_x, σ_y, σ_z are the three Pauli matrices. The band structure can thus be obtained by solving the eigen equation $H(\mathbf{k})\Psi(\mathbf{k}) = \varepsilon(\mathbf{k})\Psi(\mathbf{k})$, where $\varepsilon(\mathbf{k})$ is eigen value, $\Psi(\mathbf{k}) = (\psi_A, \psi_B)^T$ is a two-component eigen vector denoting the Bloch mode amplitude in the sublattices A and B, respectively. The cubic Brillouin zone is shown in Fig. 1(c) where $\mathbf{k} = (k_x, k_y, k_\omega)$ with $k_x, k_y \in (-\pi/a, \pi/a)$ and $k_\omega \in (-\pi/\Omega, \pi/\Omega)$. Analogous to the in-plane Bloch wave vectors k_x and k_y which denote the phase difference between neighbor spatial lattice sites, the frequency-domain wave vector k_ω also denotes the phase difference of Bloch mode amplitudes in adjacent frequency lattice sites. $\Delta\phi = \phi_2 - \phi_1$ is the phase difference of modulation in A and B waveguides. Since the phase difference is gauge invariant that doesn't rely on the explicit choices of ϕ_1 and ϕ_2, we can choose $\phi_1 = 0$ and $\phi_2 = \Delta\phi$.
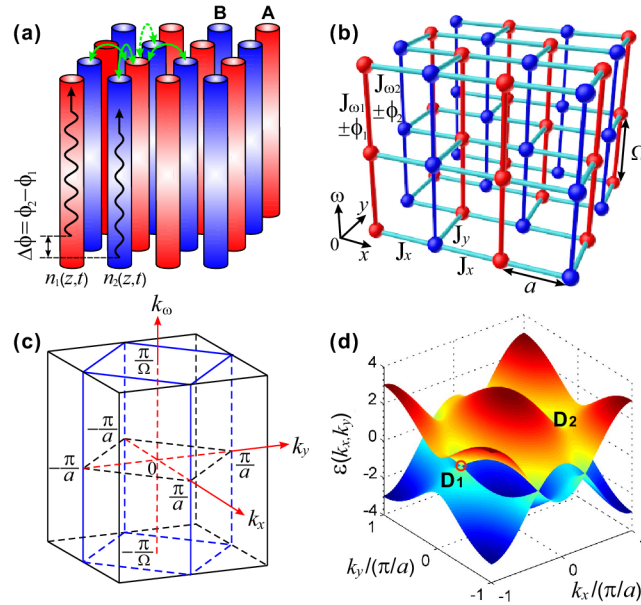

Fig. 1. (a) Schematic diagram of a dynamically modulated brick-wall waveguide array consisting of evanescently coupled waveguide A (red) and B (blue) arranged in a square lattice. One of the four coupling bonds is blocked (denoted by the green dashed arrow). Both A and B waveguides are subject to the travelling-wave index modulation $n_{1(2)}(z, t)$ with phase difference $\Delta\phi = \phi_2 - \phi_1$. (b) Equivalent lattice model which consists of the in-plane brick-wall lattice and perpendicular frequency lattice, with lattice constants a and Ω. The in-plane coupling coefficients J_x and J_y have real values and frequency-domain coupling coefficients are complex values with amplitudes $J_{\omega 1}$ ($J_{\omega 2}$) and phases $\pm \phi_1$ ($\pm \phi_2$) in waveguides A and B. (c) The Brillouin zone (mark in blue) for the equivalent lattice of (b), with $k_x, k_y \in (-\pi/a, \pi/a)$ and $k_\omega \in (-\pi/\Omega, \pi/\Omega)$. (d) Projected band structure $\varepsilon(k_x, k_y)$ for the brick-wall lattice in the absence of dynamic modulation. D_1, D_2 denotes two Dirac points by choosing $a = 1$ and $J_x = J_y$.

For WPs to emerge, either inversion (P) or time-reversal (T) symmetry should be broken [1–6,13–21]. To break P and preserve T, we can choose $J_{\omega 1} \neq J_{\omega 2}$ and $\Delta\phi = 0$ (or π). To break T and preserve P, we should keep $J_{\omega 1} = J_{\omega 2}$ and choose $\Delta\phi \neq 0$ (or π). To break both P and T, we keep $J_{\omega 1} \neq J_{\omega 2}$ and choose $\Delta\phi \neq 0$ and $\Delta\phi \neq \pi$. Before discussing the WPs, we firstly consider the Dirac points for the 2D brick-wall lattice in the absence of dynamic modulation. From Eq. (3), we have the 2D Hamiltonian

$$H_{2D}(\mathbf{k}) = [2J_x \cos(k_x a) + J_y \cos(k_y a)]\sigma_x + J_y \sin(k_y a)\sigma_y, \tag{4}$$

where we assume the Dirac points locate at (k_{x0}, k_{y0}), near which the Bloch wave vectors are $k_x = k_{x0} + q_x$ and $k_y = k_{y0} + q_y$. In the vicinity of Dirac points, the Hamiltonian of Eq. (3) should take the form of $H_D(\boldsymbol{q}) = q_x v_x \sigma_x + q_y v_y \sigma_y$, so we can obtain $k_{y0} = 0$. Equation (4) thus reads

$$H_{2D}(\mathbf{q}) = [2J_x \cos(k_{x0}a) + J_y]\sigma_x - 2J_x \sin(k_{x0}a)q_x a\sigma_x + J_y q_y a\sigma_y, \tag{5}$$

where k_{x0} should satisfy the condition of $2J_x\cos(k_{x0}a) + J_y = 0$. So if the coupling coefficients satisfy $|J_y| > |2J_x|$, k_{x0} doesn't exist. On the contrary, if $|J_y| \leq |2J_x|$, the Dirac points locate at $k_{x0} = \pm [\pi - \arccos(J_y/2J_x)]/a$. The Dirac Hamiltonian can be rewritten as

$$H_{2D}(\mathbf{q}) = \pm v_x q_x \sigma_x + v_y q_y \sigma_y, \tag{6}$$

where the in-plane group velocities are given by

$$\begin{cases} v_x = -\sqrt{4J_x^2 - J_y^2}\, a \\ v_y = J_y a \end{cases} \tag{7}$$

In Fig. 1(d), we numerically calculate the projected band structure $\varepsilon(k_x, k_y)$ by using the Hamiltonian in Eq. (4). By choosing $a = 1$ and $J_x = J_y$, we can obtain two Dirac points at $D_{1,2}(\pm 2\pi/3, 0)$. Based on the Dirac points, we construct WPs by adding a synthetic frequency dimension in the presence of dynamic modulation.

For the P-symmetry broken case with $J_{\omega 1} \neq J_{\omega 2}$ and $\Delta\phi = 0$ (or π), the 3D Hamiltonian is

$$H(\mathbf{k}) = H_{2D}(\mathbf{k}) + \begin{cases} \cos(k_\omega \Omega)(J_{\omega 1} - J_{\omega 2})(\sigma_z + \tau\sigma_0), & (\Delta\phi = 0) \\ \cos(k_\omega \Omega)(J_{\omega 1} + J_{\omega 2})(\sigma_z + \dfrac{1}{\tau}\sigma_0), & (\Delta\phi = \pi) \end{cases} \tag{8}$$

where $\tau = (J_{\omega 1} + J_{\omega 2})/(J_{\omega 1} - J_{\omega 2})$. We assume the WPs locate at $k_{\omega 0}$ in the reciprocal space of frequency dimension with $k_\omega = k_{\omega 0} + q_\omega$. In the vicinity of WPs, the dispersion relation should be linear, which indicates $k_{\omega 0} = \pm (\pi/2\Omega)$. So there are four WPs at $(\pm [\pi - \arccos(J_y/2J_x)]/a, 0, \pm \pi/2\Omega)$ in the 3D Brillouin zone, near which the Weyl Hamiltonian is

$$H_W(\mathbf{q}) = \pm v_x q_x \sigma_x + v_y q_y \sigma_y \pm \begin{cases} v_{\omega,0} q_\omega (\sigma_z + \tau\sigma_0), & (\Delta\phi = 0) \\ v_{\omega,\pi} q_\omega (\sigma_z + \dfrac{1}{\tau}\sigma_0), & (\Delta\phi = \pi) \end{cases} \tag{9}$$

where $v_{\omega,0} = -(J_{\omega 1} - J_{\omega 2})\Omega$, and $v_{\omega,\pi} = -(J_{\omega 1} + J_{\omega 2})\Omega$ are the group velocities along the frequency dimension as $\Delta\phi = 0$ or π, respectively. Note that the coupling strengths $J_{\omega 1}$ and $J_{\omega 2}$ have the same signs, which indicate $|\tau| > 1$. So the in-phase modulation $\Delta\phi = 0$ can generate Type-II WPs and out-of-phase modulation $\Delta\phi = \pi$ can generate Type-I WPs [6,7].

For the cases of T-symmetry or PT-symmetry broken case with $\Delta\phi \neq 0$ and $\Delta\phi \neq \pi$, the $\boldsymbol{k}$-space Hamiltonian is

$$H(\mathbf{k}) = [2J_x \cos(k_x a) + J_y \cos(k_y a)]\sigma_x + J_y \sin(k_y a)\sigma_y$$
$$- \sqrt{J_{\omega 1}^2 - 2J_{\omega 1}J_{\omega 2}\cos(\Delta\phi) + J_{\omega 2}^2}\,\sin(k_\omega\Omega - \alpha)\sigma_z \qquad (10)$$
$$+ \sqrt{J_{\omega 1}^2 + 2J_{\omega 1}J_{\omega 2}\cos(\Delta\phi) + J_{\omega 2}^2}\,\sin(k_\omega\Omega + \beta)\sigma_0,$$

where α and β satisfy

$$\tan(\alpha) = \frac{J_{\omega 1} - J_{\omega 2}\cos(\Delta\phi)}{J_{\omega 2}\sin(\Delta\phi)}, \quad \tan(\beta) = \frac{J_{\omega 1} + J_{\omega 2}\cos(\Delta\phi)}{J_{\omega 2}\sin(\Delta\phi)}, \qquad (11)$$

The WPs locate at $k_{\omega 0} = \alpha/\Omega$ and $k_{\omega 0} = (\alpha - \pi)/\Omega$, with the Weyl Hamiltonian W_1 given by

$$H_{W_1}(\mathbf{q}) = v_x q_x \sigma_x + v_y q_y \sigma_y + v_\omega q_\omega \sigma_z$$
$$+ \varepsilon_0 \sigma_0 + v_0 q_\omega \sigma_0 + \varepsilon_0 \sigma_0 [-\frac{1}{2}q_\omega^2\Omega^2 + \mathrm{o}(q_\omega^2\Omega^2)], \qquad (12)$$

with the group velocities v_ω, v_0 and the energy at WPs ε_0 given by

$$\begin{cases} v_\omega = -\sqrt{J_{\omega 1}^2 - 2J_{\omega 1}J_{\omega 2}\cos(\Delta\phi) + J_{\omega 2}^2}\,\Omega \\ v_0 = \cos(\alpha + \beta)\sqrt{J_{\omega 1}^2 + 2J_{\omega 1}J_{\omega 2}\cos(\Delta\phi) + J_{\omega 2}^2}\,\Omega, \\ \varepsilon_0 = \sin(\alpha + \beta)\sqrt{J_{\omega 1}^2 + 2J_{\omega 1}J_{\omega 2}\cos(\Delta\phi) + J_{\omega 2}^2} \end{cases} \qquad (13)$$

The corresponding energy spectra of two bands are thus denoted by

$$\varepsilon_\pm(\mathbf{q}) = \varepsilon_0 + v_0 q_\omega + \varepsilon_0 [-\frac{1}{2}q_\omega^2\Omega^2 + \mathrm{o}(q_\omega^2\Omega^2)] \pm \sqrt{v_x^2 q_x^2 + v_y^2 q_y^2 + v_\omega^2 q_\omega^2}, \qquad (14)$$

where "+" and "−" denotes the upper and lower bands. To distinguish between the two types of WPs, we decompose the Hamiltonian of Eq. (12) into $H_{W1}(\mathbf{q}) = \varepsilon_0\sigma_0 + H_U(\mathbf{q}) + H_T(\mathbf{q})$, with

$$\begin{cases} H_U(\mathbf{q}) = v_x q_x \sigma_x + v_y q_y \sigma_y + v_\omega q_\omega \sigma_z \\ H_T(\mathbf{q}) = v_0 q_\omega \sigma_0 + \varepsilon_0 \sigma_0 [-\frac{1}{2}q_\omega^2\Omega^2 + \mathrm{o}(q_\omega^2\Omega^2)] \end{cases} \qquad (15)$$

where $H_U(\mathbf{q})$ and $H_T(\mathbf{q})$ constitute the potential and kinetic energy components of $H_{W1}(\mathbf{q})$. The total energy spectrum $\varepsilon_\pm(\mathbf{q})$ can thus be decomposed into the constant energy component of ε_0, potential and kinetic energy spectra $U(\mathbf{q})$ and $T(\mathbf{q})$, with

$$\begin{cases} U(\mathbf{q}) = \sqrt{v_x^2 q_x^2 + v_y^2 q_y^2 + v_\omega^2 q_\omega^2} \\ T(\mathbf{q}) = \varepsilon_\pm(\mathbf{q}) - \varepsilon_0 - U(\mathbf{q}) \end{cases} \qquad (16)$$

For the WPs to be of Type-I, $U(\mathbf{q}) > T(\mathbf{q})$ should be satisfied in all directions of $\mathbf{q}$. On the contrary, if there exists a particular direction along which $T(\mathbf{q})$ dominates over $U(\mathbf{q})$ with $T(\mathbf{q}) > U(\mathbf{q})$, the WPs are of Type-II [7]. So the system exhibits a phase transition between Type-I to Type-II WPs at $T(\mathbf{q}) = U(\mathbf{q})$. The phase transition point can be obtained by comparing $T(\mathbf{q})$ and $U(\mathbf{q})$ numerically. At the phase transition point, the group velocities of two bands in frequency dimension are given by

$$v_{g,\pm}^\omega(\mathbf{q}) = \frac{\partial \varepsilon_\pm(\mathbf{q})}{\partial q_\omega} = v_0 + \varepsilon_0 [-q_\omega\Omega^2 + \mathrm{o}(q_\omega\Omega^2)] \pm \frac{q_\omega v_\omega^2}{\sqrt{v_x^2 q_x^2 + v_y^2 q_y^2 + v_\omega^2 q_\omega^2}}, \qquad (17)$$

In the vicinity of WPs with $q_x = q_y = 0$, the group velocities can be reduced to

$$v_{g,\pm}^{\omega}(0,0,q_\omega) = v_0 + \varepsilon_0[-q_\omega\Omega^2 + o(q_\omega\Omega^2)] \pm v_\omega, \qquad (18)$$

from which we have $v_{g,\pm}^{\omega}(0,0,q_\omega \to 0) = v_0 \pm v_\omega$. For Type-I WPs, the group velocities of two bands should have the opposite directions, which means $|v_0| < |v_\omega|$. On the contrary for Type-II WPs, the two group velocities should have the same directions, such that $|v_0| > |v_\omega|$. So at the phase transition point, the group velocity satisfies $|v_0| = |v_\omega|$. Without loss of generality, we assume $v_0 = v_\omega$, the two group velocities will become

$$\begin{cases} v_{g,+}^{\omega}(0,0,q_\omega \to 0) = v_0 + v_\omega \\ v_{g,-}^{\omega}(0,0,q_\omega \to 0) = 0 \end{cases}, \qquad (19)$$

It shows that one of the band will become flat in the vicinity of WPs with zero group velocity while the other band has finite group velocity. So the local flat band structure is a physical signature of phase transition occurring at the boundaries between Type-I and Type-II WPs.
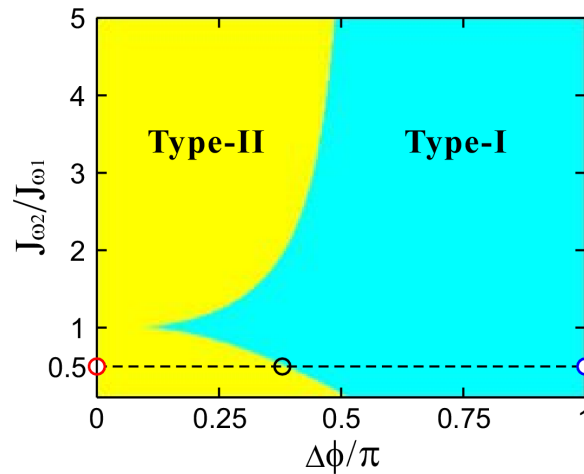

Fig. 2. Phase diagram for Type-I and Type-II Weyl points versus the modulation phase difference $\Delta\phi = \phi_2 - \phi_1$ and coupling strength ratio $J_{\omega2}/J_{\omega1}$. In the simulation, we fix $J_{\omega2}/J_{\omega1} = 0.5$ as denoted by the black dashed line. The red and blue circles represent the situations of in-phase ($\Delta\phi = 0$) and out-of-phase modulations ($\Delta\phi = \pi$), respectively. Black circle denotes $\Delta\phi = 0.383\pi$, which denotes the transition point between Type-I and Type-II WPs.

Figure 2 shows the phase diagram for Type-I and Type-II WPs versus the modulation phase difference $\Delta\phi$ and coupling strength ratio $J_{\omega2}/J_{\omega1}$. The phase diagram is an important tool widely used in condensed-matter physics to characterize the system properties in a continuously varying parameter space. From the phase diagram, we can obtain the precise boundary at which the system experiences an abrupt transition from Type-I to Type-II WPs or vice versa. Note that both the coupling strength ratio and modulation phase difference are controlled by external modulation, we can thus realize Weyl phase transition by continuously varying the modulation parameters without changing the lattice structure. The phase transition is more readily to realize than the previously proposed methods of lattice strain or anisotropic couplings [22,23]. For an arbitrary choice of $J_{\omega2}/J_{\omega1}$, the WPs are of Type-I as $\Delta\phi$ is chosen in the vicinity of π and Type-II as $\Delta\phi$ approaches 0. For sufficiently small or large $J_{\omega2}/J_{\omega1}$, the Weyl phase transition occurs at $\Delta\phi = \pi/2$. For a general $J_{\omega2}/J_{\omega1}$, the phase transition point varies from $\pi/2$ to 0. Specifically for $J_{\omega2} = J_{\omega1}$, the phase difference reaches the minimum value of $\Delta\phi = 0.098\pi$ as the phase transition occurs. In the following, we will fix $J_{\omega2}/J_{\omega1} = 0.5$

and choose $\Delta\phi = 0$, π and the phase transition point of 0.383π to demonstrate both two types of WPs, as denoted by the red, blue and black circles in Fig. 2.

Firstly, we consider Type-I WPs for the out-of-phase modulation $\Delta\phi = \pi$ where the projected band structures and isoenergy contours are shown in Fig. 3. Throughout the paper we choose $a = \Omega = 1$ and isotropic in-plane coupling strengths $J_x = J_y$. The coupling strengths in the frequency dimension are $J_{\omega1} = 1$ and $J_{\omega2} = 0.5$. The projected band structure $\varepsilon(k_x, k_\omega)$ at $k_y = k_{y0} = 0$ is shown in Fig. 3(a), where there exist four WPs of W_1, W_2, W_3, and W_4 locating at ($\pm 2\pi/3$, $\pm \pi/2$) in the k_x-k_ω plane. Figures 3(b) and 3(c) illustrate the isoenergy contours for the upper and lower bands of the projected band structure. In the vicinity of each WP, the isoenergy contour is closed and takes the shape of an ellipse, verifying that it is of Type-I. The sign "+" or "−" at each WP denotes its chirality, which is characterized by the sign of Chern number $c = \text{sgn}[\det(v_x v_y v_\omega)]$ [13]. So we have $c = 1$ for W_1, W_3 and $c = -1$ for W_2 and W_4, which represent the "source" and "sink" of Berry flux. Figure 3(d) shows the projected band structure $\varepsilon(k_y, k_\omega)$ at $k_{x0} = 2\pi/3$, in which $W_{1(2)}$, $W_{4(3)}$ locate at $(0, \pm \pi/2)$ in the k_x-k_ω plane. The corresponding isoenergy contours of upper and lower bands are shown in Figs. 3(e) and 3(f). In the vicinity of each WP, the contour is elliptic, which further verify that it is of Type-I.
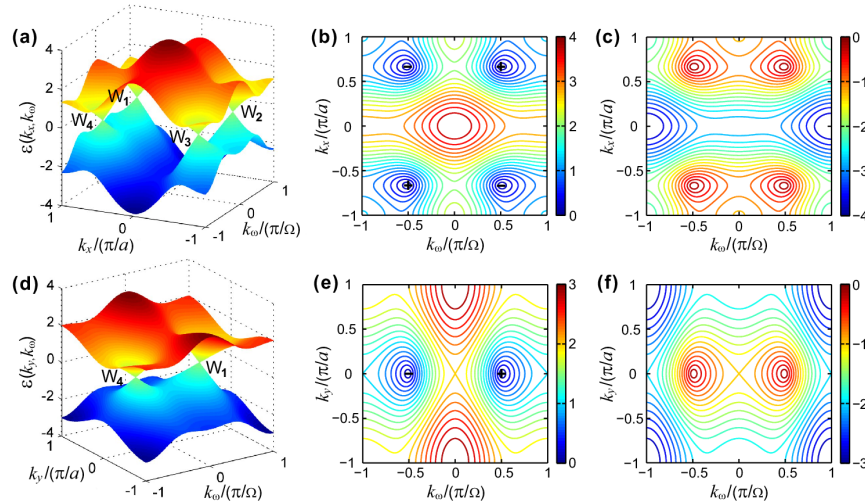

Fig. 3. Projected band structures and isoenergy contours for Type-I WPs under $\Delta\phi = \pi$. (a) Projected band structure $\varepsilon(k_x, k_\omega)$ at $k_{y0} = 0$ with W_1, W_2, W_3, and W_4 locating at ($\pm 2\pi/3$, $\pm \pi/2$). The parameters are $a = \Omega = 1$, $J_x = J_y = J_{\omega1} = 1$ and $J_{\omega2} = 0.5$. (b) (c) Isoenergy contours for the upper and lower bands of the projected band structure of (a). The signs "+" and "−" denote the sign of the Chern number for each WP. (b) Projected band structure $\varepsilon(k_y, k_\omega)$ at $k_{x0} = 2\pi/3$ with $W_{1(2)}$, $W_{4(3)}$ locating at $(0, \pm \pi/2)$. (e) (f) Isoenergy contours for the upper and lower bands.

In Fig. 4, we choose in-phase modulation $\Delta\phi = 0$ and keep other parameters the same with those in Fig. 3. In the projected band structure $\varepsilon(k_x, k_\omega)$ at $k_y = 0$, as shown in Fig. 4(a), the four WPs locate at ($\pm 2\pi/3$, $\pm \pi/2$) in the k_x-k_ω plane, which are also the same with those in Fig. 3(a). The isoenergy contours for the upper and lower bands of the projected band structure are shown in Figs. 4(b) and 4(c). The isoenergy contour is open and hyperbolic in the vicinity of each WP, thus verifying that it is of Type-II. Note that though the type has experienced a transition from Type-I to Type-II, the chiralities of all WPs keep unchanged. This is because chirality and type are two independent properties of WPs: the chirality denotes the topological charge while the type reflects local shape of the two bands. The projected band structure $\varepsilon(k_y, k_\omega)$ at $k_{x0} = 2\pi/3$ is shown in Fig. 4(d), with $W_{1(2)}$, $W_{4(3)}$ locating

at $(0, \pm \pi/2)$. The isoenergy contours for the upper and lower bands are shown in Figs. 4(e) and 4(f), which also exhibit open hyperbolic shape in the vicinity of each WP.
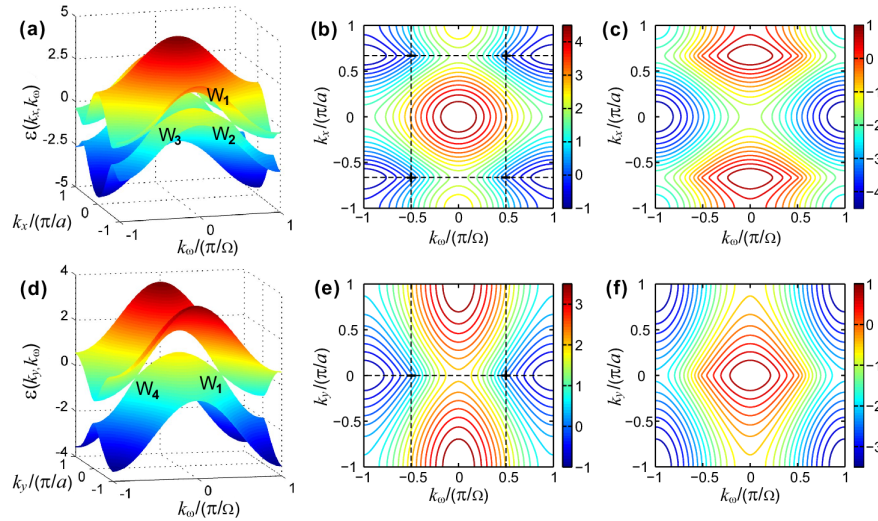

Fig. 4. Projected band structures and isoenergy contours for Type-II WPs under $\Delta\phi = 0$. All other parameters are kept the same with those in Fig. 3. (a) Projected band structure $\varepsilon(k_x, k_\omega)$ at $k_{y0} = 0$ with four WPs W_1, W_2, W_3, and W_4 locating at ($\pm 2\pi/3, \pm \pi/2$). (b) (c) Isoenergy contours for the upper and lower bands, with the signs "+" and "−" at each WP denotes its chirality. (b) Projected band structure $\varepsilon(k_y, k_\omega)$ at $k_{x0} = 2\pi/3$ with $W_{1(2)}$, $W_{3(4)}$ locating at $(0, \pm \pi/2)$. (e) (f) Isoenergy contours for the upper and lower bands of the projected band structure in (d).
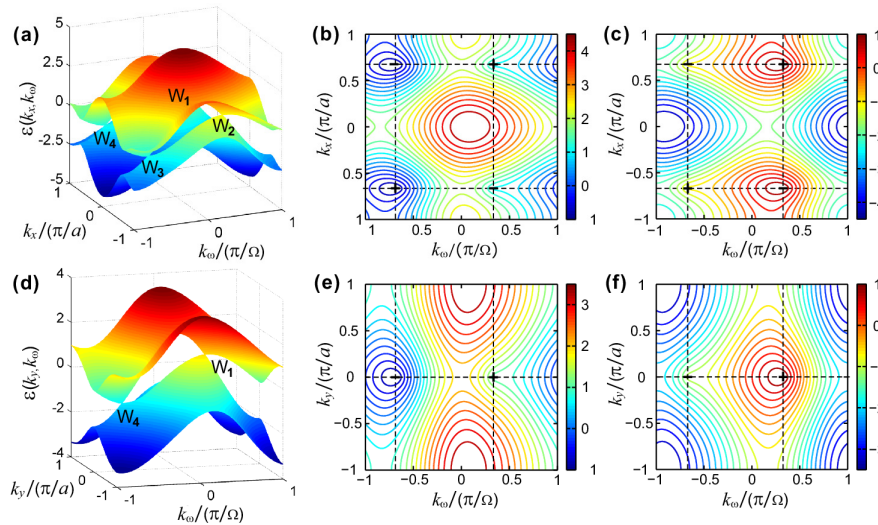

Fig. 5. Projected band structures and isoenergy contours at the phase transition point of $\Delta\phi = 0.383\pi$. (a) Projected band structure $\varepsilon(k_x, k_\omega)$ at $k_{y0} = 0$ with the four WPs locating at $k_{\omega 0} = 0.335\pi$ and -0.665π. (b) (c) Isoenergy contours where the signs "+" and "−" at each WP denotes its chirality. (b) Projected band structure $\varepsilon(k_y, k_\omega)$ at $k_{x0} = 2\pi/3$ with $W_{1(2)}$, $W_{3(4)}$ locating at $k_{\omega 0} = 0.335\pi$ and -0.665π at $\varepsilon_0 = \pm 0.989$, respectively. (e) (f) Isoenergy contours for the upper and lower bands of the projected band structure in (d).

Next we consider the phase transition point with $\Delta\phi = 0.383\pi$ where PT-symmetry is broken. The projected band structure $\varepsilon(k_x, k_\omega)$ at $k_y = 0$ is shown in Fig. 5(a). Differing from the above P-symmetry broken case under $\Delta\phi = 0$ or π with $\varepsilon(k_x, k_\omega) = \varepsilon(k_x, -k_\omega)$, the band

structure here is asymmetric with $\varepsilon(k_x, k_\omega) \neq \varepsilon(k_x, -k_\omega)$ due to the T-symmetry broken along the frequency dimension. Also, unlike the cases of $\Delta\phi = 0$ or π, in which each WP pair has equal energy $\varepsilon(k_{x0}, k_{\omega 0}) = 0$ at $k_{\omega 0} = \pm \pi/2$, the WPs migrate both in energy and momentum axes. For $J_{\omega 2}/J_{\omega 1} = 0.5$ and $\Delta\phi = 0.383\pi$, we have $k_{\omega 0} = \alpha = 0.335\pi$. So $W_{1,2}$ locates at ($\pm 2\pi/3$, 0.335π) with energy $\varepsilon = 0.989$ and $W_{3,4}$ locates at ($\pm 2\pi/3$, -0.665π) with $\varepsilon = -0.989$. Differing from Figs. 3 and 4 where the isoenergy contours near WPs are hyperbolic (or elliptical) from both upper and lower bands, the isoenergy contour in Figs. 5(b) or 5(c) near W_1 is hyperbolic from the upper band and elliptical from the lower band, indicating the asymmetry of projected band structure. This asymmetry also holds for other WPs. The projected band structure $\varepsilon(k_y, k_\omega)$ at $k_{x0} = 2\pi/3$ is shown in Fig. 5(d), which clearly shows the shift of WPs in both the energy and momentum axes. The isoenergy contours are shown in Figs. 5(e) and 5(f), in which the contour shape differs in the upper and lower bands, respectively.

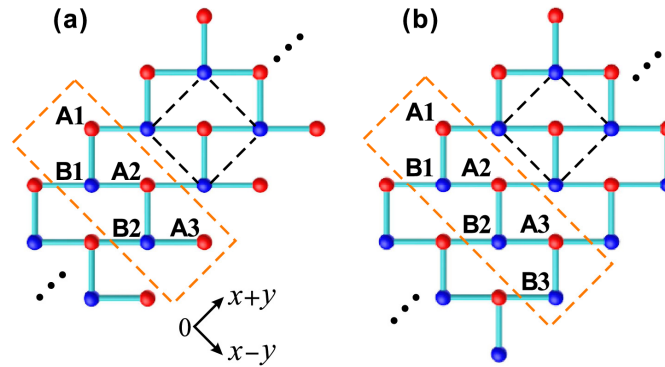## 3. Photonic Fermi-arc surface states in the truncated lattice

Fig. 6. Schematic diagrams of the A-A (left) and A-B (right) truncated lattice structures. The lattice is truncated along ($x - y$) direction and kept periodic along ($x + y$) direction and the frequency dimension. The orange dashed rectangles denote a unit cell for the truncated lattice, which contains odd and even number of waveguides for A-A and A-B lattices, respectively. The black dashed squares denote the primitive cell for the in-plane brick-wall lattice.

One important signature of Weyl semimetals is the existence of surface states at the edges of a truncated sample. The surface states manifest as open curves that connect the WPs in the projected band structure, which are termed as Fermi arcs [6–10]. As shown in Fig. 6, the array can be truncated in the ($x - y$) direction and kept periodic in the ($x + y$) direction and frequency axis. As shown in Figs. 6(a) and 6(b), there exist two kinds of truncated arrays in which the two boundaries contain the same (A-A) and different (A-B) waveguides, respectively. Here we denote them as A-A and A-B types of arrays. There are total odd and even number of waveguides in each unit cell for A-A and A-B types of array. To calculate the Fermi arc surface states, we choose the A-B type array as an example, the method of which is also applicable to A-A type array. The Hamiltonian of A-B type array is

$$H_{\mathrm{AB}} = \sum_{p,n} \left(J_x a_{1,p,n}^\dagger b_{1,p+1,n} + J_y a_{1,p,n}^\dagger b_{1,p,n} + h.c. \right)$$

$$+ \sum_{m=2,p,n}^{M} \left(J_x a_{m,p,n}^\dagger b_{m,p+1,n} + J_x a_{m,p,n}^\dagger b_{m-1,p,n} + J_y a_{m,p,n}^\dagger b_{m,p,n} + h.c. \right) \qquad (20)$$

$$+ \sum_{m=1,p,n}^{M} \left(J_{\omega 1} e^{-i\phi_1} a_{m,p,n}^\dagger a_{m,p,n+1} + J_{\omega 2} e^{-i\phi_2} b_{m,p,n}^\dagger b_{m,p,n+1} + h.c. \right),$$

where p, n are the cell indices along $(x + y)$ and frequency axes. $m = 1, 2, \dots, M$ denotes the site index in a unit cell along $(x - y)$ direction with $2M$ being the total waveguide number in each unit cell. The k-space Hamiltonian is thus given by

$$
\begin{aligned}
H_{AB} = & \sum_{\mathbf{k}} \left(J_x e^{ik_p \sqrt{2}a} + J_y \right) a_{1,\mathbf{k}}^{\dagger} b_{1,\mathbf{k}} + \sum_{\mathbf{k}} \left(J_x e^{-ik_p \sqrt{2}a} + J_y \right) b_{1,\mathbf{k}}^{\dagger} a_{1,\mathbf{k}} \\
& + \sum_{m=2,\mathbf{k}}^{M} \left[\left(J_x e^{ik_p \sqrt{2}a} + J_y \right) a_{m,\mathbf{k}}^{\dagger} b_{m,\mathbf{k}} + \left(J_x e^{-ik_p \sqrt{2}a} + J_y \right) b_{m,\mathbf{k}}^{\dagger} a_{m,\mathbf{k}} + J_x a_{m,\mathbf{k}}^{\dagger} b_{m-1,\mathbf{k}} + J_x b_{m-1,\mathbf{k}}^{\dagger} a_{m,\mathbf{k}} \right] \quad (21) \\
& + \sum_{m=1,\mathbf{k}}^{M} \left[\left(J_{\omega 1} e^{-i\phi_1} e^{ik_\omega \Omega} + J_{\omega 1} e^{i\phi_1} e^{-ik_\omega \Omega} \right) a_{m,\mathbf{k}}^{\dagger} a_{m,\mathbf{k}} + \left(J_{\omega 2} e^{-i\phi_2} e^{ik_\omega \Omega} + J_{\omega 2} e^{i\phi_2} e^{-ik_\omega \Omega} \right) b_{m,\mathbf{k}}^{\dagger} b_{m,\mathbf{k}} \right],
\end{aligned}
$$

where $\mathbf{k} = (k_p, k_\omega)$ is the Bloch momentum along $(x + y)$ and frequency axes. By denoting

$$
H_{AB} = \left(a_{1,\mathbf{k}}^{\dagger}\ b_{1,\mathbf{k}}^{\dagger}\ a_{2,\mathbf{k}}^{\dagger}\ b_{2,\mathbf{k}}^{\dagger} \dots a_{m,\mathbf{k}}^{\dagger}\ b_{m,\mathbf{k}}^{\dagger} \right) H_{AB}(\mathbf{k}) \left(a_{1,\mathbf{k}}\ b_{1,\mathbf{k}}\ a_{2,\mathbf{k}}\ b_{2,\mathbf{k}} \dots a_{m,\mathbf{k}}\ b_{m,\mathbf{k}} \right)^{\mathrm{T}}, \quad (22)
$$

we can obtain the Bloch Hamiltonian, which is given by a $2M \times 2M$ matrix

$$
H_{AB}(\mathbf{k}) = \begin{pmatrix}
2J_{\omega 1}\cos(k_\omega \Omega - \phi_1) & J_x e^{ik_p \sqrt{2}a} + J_y & 0 & \cdots & 0 & 0 \\
J_x e^{-ik_p \sqrt{2}a} + J_y & 2J_{\omega 2}\cos(k_\omega \Omega - \phi_2) & J_x & \cdots & 0 & 0 \\
0 & J_x & 2J_{\omega 1}\cos(k_\omega \Omega - \phi_1) & \cdots & 0 & 0 \\
\vdots & \vdots & \vdots & \ddots & 0 & 0 \\
0 & 0 & 0 & \cdots & 2J_{\omega 1}\cos(k_\omega \Omega - \phi_1) & J_x e^{ik_p \sqrt{2}a} + J_y \\
0 & 0 & 0 & \cdots & J_x e^{-ik_p \sqrt{2}a} + J_y & 2J_{\omega 2}\cos(k_\omega \Omega - \phi_2)
\end{pmatrix} \quad (23)
$$

with the eigen state denoted by the unit-cell mode amplitude $\Psi = (\psi_{A1}, \psi_{B1}, \psi_{A2}, \psi_{B2}, \dots, \psi_{AN}, \psi_{AN})$. So the projected band structure $\varepsilon(\mathbf{k})$ can be obtained by solving $H_{AB}(\mathbf{k})\Psi = \varepsilon(\mathbf{k})\Psi$.
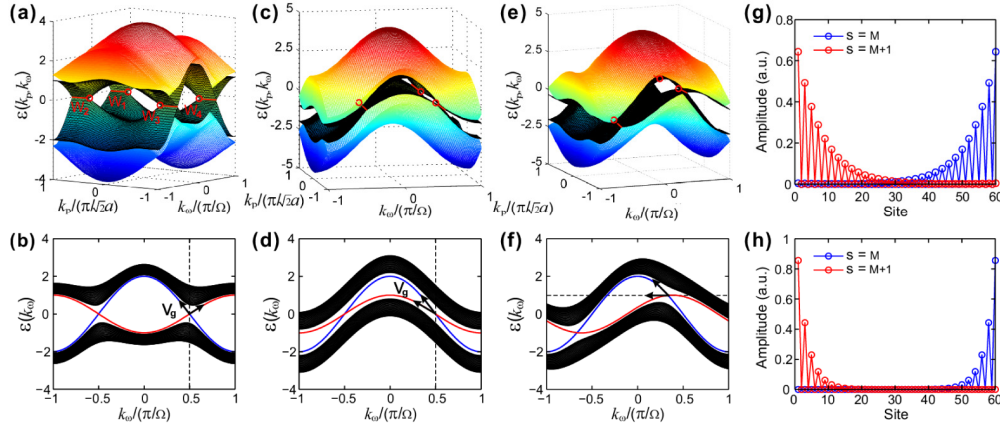

Fig. 7. (a) Projected band structure of Type-I WPs for the A-B truncated array under $\Delta\phi = \pi$. The two surface states are denoted by the green surfaces and the red (blue) surfaces are the bulk bands. The red circles represent the four WPs connected by the Fermi arcs denoted by the red lines. (b) A sliced projected band structure at $k_p = 5\pi/6$ with the black arrows denoting the group velocities of the two surface states. (c) Projected band structure of Type-II WPs under $\Delta\phi = 0$. (d) Sliced projected band structure at $k_p = 5\pi/6$. (e) Projected band structure of Type-II WPs with $\Delta\phi = 0.383\ \pi$. (f) Sliced projected band structure at $k_p = 5\pi/6$. (g) (h) Eigen-mode amplitudes for the two surface states as $k_p = 3\pi/4$ and $5\pi/6$ under $\Delta\phi = \pi$ and $k_\omega = \pi/2$.

Figure 7(a) shows the projected band structure $\varepsilon(k_p, k_\omega)$ of A-B type truncated array for Type-I WPs under $\Delta\phi = \pi$. Here we choose $2M = 60$ waveguides in each unit cell, thus there are totally 60 bands of $s = 1, 2, \dots, 60$, where s is the band index. The bands $s = M$ and $s = M + 1$ represent the edge states while others denote the bulk bands. The two edge states intersect to form four line segments (denoted by red solid lines), forming the Fermi arcs that connect the four WPs at $k_p = \pm 2\pi/3$, $k_\omega = \pm \pi/2$ denoted by the red circles. In Fig. 7(b), we plot the a

slice of the projected band structure $\varepsilon(k_\omega)$ at $k_p = 5\pi/6$ where the red and blue curves denote the two edge states that are isolated from the bulk bands (denoted by black curves). For an arbitrary choice of k_ω, as shown by the black arrows, the two edge states propagate in opposite directions with opposite group velocities at the upper and lower boundaries, respectively. Figure 7(c) shows the projected band structure for Type-II WPs with $\Delta\phi = 0$, where the positions of Fermi arcs are the same with those in Fig. 7(a). The sliced projected band structure $\varepsilon(k_\omega)$ at $k_p = 5\pi/6$ is shown in Fig. 7(d). Differing from Type-I WPs for which the two edge states have opposite group velocities at a specific k_ω, the two edge states for Type-II WPs propagate in the same directions at different boundaries. In this regard, the optical modes of the surface states will experience bidirectional and unidirectional frequency shift in Type-I and Type-II WPs. In Figs. 7(e) and 7(f), we plot the projected band structures at the phase transition point of $\Delta\phi = 0.383\pi$. As is shown in Fig. 7(e), one of the surface state manifests flat dispersion relation with vanished group velocity along the frequency dimension. The local flat band structure is an important physical signature at the phase transition point. Additionally, since T-symmetry is broken, the projected band structure exhibits $\varepsilon(k_p, k_\omega) \neq \varepsilon(k_p, -k_\omega)$ for both edge and bulk bands. In Figs. 7(g) and 7(h), we plot the mode amplitude for the two edge states $s = M$ and $s = M + 1$, by choosing $k_p = 3\pi/4$ and $5\pi/6$ with $\Delta\phi = \pi$ and $k_\omega = \pi/2$. The edge states are both confined at the two boundaries, which penetrate into the bulk exponentially along the truncated directions. As k_p is chosen more closer to the WPs, the edge states can be weakly confined to the surfaces with larger penetration depths along the truncated directions.
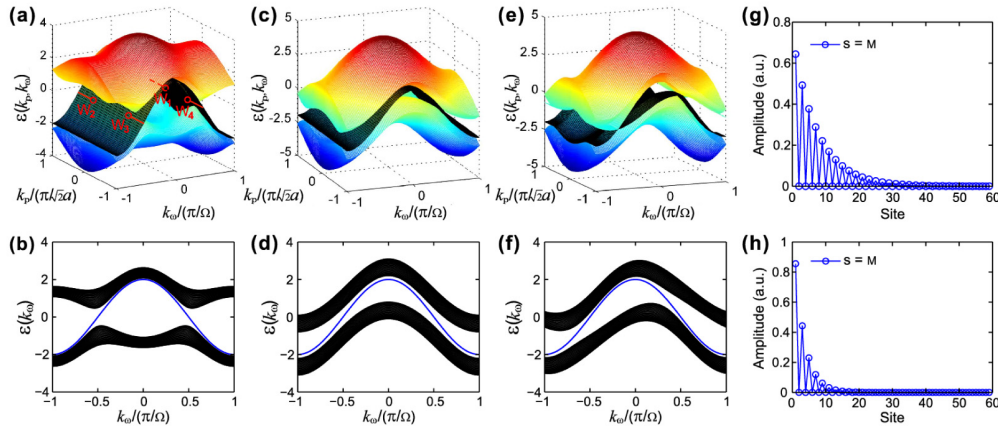

Fig. 8. (a) Projected band structure of Type-I WPs for A-A type array under $\Delta\phi = \pi$. The green surface denotes the only surface state and the red (blue) surfaces denote the bulk bands. (b) The sliced projected band structure at $k_p = 5\pi/6$. (c) (d) 2D Projected band structure for Type-II WPs with $\Delta\phi = 0$ and sliced projected band structure at $k_p = 5\pi/6$. (e) (f) 2D projected band structure at $\Delta\phi = 0.383\pi$ and sliced projected band structure at $k_p = 5\pi/6$. (g) (h) Eigen-mode amplitudes for the only surface state as $k_p = 3\pi/4$ and $5\pi/6$ under $\Delta\phi = \pi$ and $k_\omega = \pi/2$.

Then we turn to A-A type truncated array. Figure 8(a) shows the projected band structure for Type-I WPs under $\Delta\phi = \pi$. There are totally $2M - 1$ bands denoted as $s = 1, 2, ..., 2M - 1$, among which the band $s = M$ is the only surface state with others representing the bulk bands. Differing from the A-B type array that has two surface states at either the upper and lower boundaries, there is only one surface state at the upper boundary of A-A type array. Similar to A-B type array, the WPs still locate on the band of surface state, as denoted by the red circles. The sliced projected band structure $\varepsilon(k_\omega)$ at $k_p = 5\pi/6$ is shown in Fig. 8(b). Here the blue curve denotes the surface state, which is isolated from bulk bands denoted by the black curves. The projected band structures for $\Delta\phi = 0$ or 0.383π are shown in Figs. (c)-(f), which also exhibit only one surface state at the upper boundary. In Figs. 8(g) and 8(h), we plot the

eigen-mode amplitudes of the surface state by choosing $k_p = 3\pi/4$ and $5\pi/6$ under $\Delta\phi = \pi$ and $k_\omega = \pi/2$. The surface states can be well confined at the upper boundary, with the penetration depth increasing as k_p is closer to the WPs.

4. Proposals to realize brick-wall waveguide arrays

Now we propose dielectric/metallic structures to realize the brick-wall lattices. As shown in Fig. 9(a), each unit cell of the brick-wall lattice is composed of a central waveguide A(B) surrounded by four B(A) waveguides arranged in a square lattice. To remove one of the four coupling bonds, we utilize a metallic slab to block the evanescent coupling between the central and upper waveguides. The field evolution for the waveguide coupling is shown in Fig. 9(b), which is obtained by numerical simulations using COMSOL Multiphysics. The refractive indices of waveguides and surrounding medium are $n_0 = 1.45$ and $n_c = 1.2$. The metallic slab is composed of Au whose dielectric constant is described by the Drude model [38–41]. We choose the operation wavelength $\lambda_0 = 1.55$ μm, such that the refractive index of Au is $n_m = 0.1894 + 11.2241i$. The radius of the waveguide and the central spacing between neighboring ones are $r = 0.5$ μm and $d = 1.5$ μm. The thickness of Au slab is $t = 50$ nm. In the simulation, we inject the fundamental mode in the z direction from the input end of the central waveguide. The central waveguide is a little longer than other waveguides to eliminate unwanted scattering from other waveguides at the input end. Figure 9(b) shows the electric field distributions at three sections of $z = 0$, 1 and 4μm, respectively. The optical mode can exhibit efficient coupling from the central A waveguide to the left, right and lower three B waveguides. On the contrary, the coupling between the central A and upper B waveguide is blocked by the Au slab in between. The simulation verify the feasibility of constructing brick-wall lattice from conventional square lattice by using dielectric/metallic waveguides.
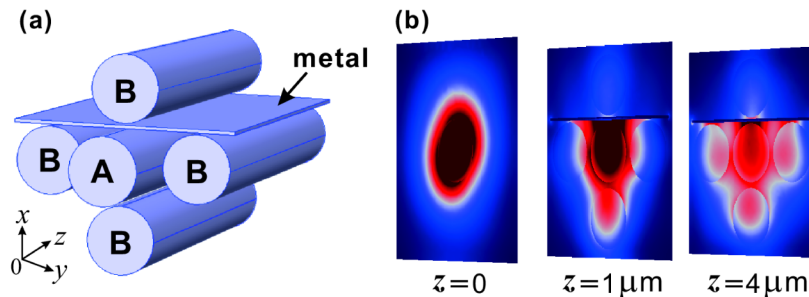

Fig. 9. (a) Schematic diagram of a unit cell for the brick-wall waveguide array. The refractive indices of the waveguide and the cladding medium are $n_0 = 1.45$ and $n_1 = 1.2$, respectively. The metallic slab is composed of Au, which is used to block the coupling between waveguide A and the upper waveguide B. (b) Simulated field distribution at different sections at $z = 0$, 1 and 4 μm under the single mode input from the central A waveguide.

For experimental implementations, the time-dependent refractive index variation may be realized with electro-optic modulations [33, 42, 43]. In detail, the required travelling-wave modulation can be provided by a sinusoidal radiofrequency (RF) signal via metallic electrodes fabricated on the surface of each waveguide. The modulation amplitudes can be controlled by using RF amplifiers and attenuators while the modulation phases can be continuously tuned by using RF phase shifters. To guarantee the precise control of modulation amplitudes and phases to achieve the phase transition, RF signals can be monitored using microwave oscilloscope for the use of feedback. Alternatively, the electro-optic modulation may also be replaced by using nonlinear optical effects of four-wave mixing (FWM) [44], in which the frequency of a signal light wave can experience up and downward transition under two pumped light waves and form a synthetic frequency lattice. The coupling amplitudes and phase difference can be controlled by varying the relative phases of the two pumped light waves in the two sublattices.

5. Conclusions

In summary, we theoretically demonstrate the phase transition between Type-I and Type-II WPs in a dynamically modulated brick-wall waveguide array. The synthetic frequency dimension created by dynamic modulation and the in-plane brick-wall lattice can constitute a synthetic 3D lattice structure. By choosing different modulation amplitudes and phases in the two sub lattices of the array, both P and T symmetries are broken and two types of WPs are formed. The out-of-phase and in-phase modulations are able to generate Type-I and Type-II WPs. For other choices of modulation phase difference and relative amplitude, we obtain the full phase diagram for the phase transition between Type-I and Type-II WPs. By truncating the brick-wall array in two different formats, we can obtain a pairwise and single Fermi arc surface states, respectively. The pairwise surfaces states of Type-I and Type-II WPs exhibit opposite and same group velocities along two boundaries, leading to the bidirectional and unidirectional frequency shifts, respectively. The study provides a unique platform to realize various Weyl semimetal phases in the same building block, enabling the efficient control over the topological wave transport in spatial and frequency domains.

Appendix: Derivation of the Hamiltonian for the 3D synthetic lattice

In the appendix, we provide the detailed derivation of the system Hamiltonian in Eq. (2). For a single-mode optical waveguide (A or B) subject to a travelling-wave modulation $n(z, t) = n_0 + \Delta n\cos(\Omega t - qz + \phi)$, the optical mode will experience photonic transitions in the fundamental band. The electric field distribution in each waveguide is $E(x, y, z, t) = \sum_n a_n(z)\psi_n(x, y)\exp[i(\omega_n t - \beta_n z)]$, where $\omega_n = \omega_0 + n\Omega$ and $\beta_n = \beta_0 + nq$ $(n = 0, \pm1, \pm2,…)$ are the frequency and propagation constant of nth-order optical mode. $a_n(z)$ and $\psi_n(x, y)$ are the corresponding mode amplitude and transverse profile, respectively. Substituting the time-dependent refractive index and electric field distributions into Maxwell's equation, we have

$$\nabla^2 E(x,y,z,t) - \frac{\varepsilon_d}{c^2}\frac{\partial^2}{\partial t^2} E(x,y,z,t) = \frac{\Delta\varepsilon}{c^2}\frac{\partial^2}{\partial t^2}\left[\cos(\Omega t - qz + \phi)E(x,y,z,t)\right], \quad (24)$$

where $\varepsilon_d = n_0^2$, $\Delta\varepsilon = 2n_0\Delta n$. By applying slowly varing amplitude approximation, the left side of Eq. (24) can be written as

$$-\sum_n 2i\beta_n \frac{\partial a_n(z)}{\partial z}\psi_n(x,y)e^{i(\omega_n t - \beta_n z)}, \quad (25)$$

By denoting $\omega_n \pm \Omega = \omega_{n\pm1}$, $\beta_n \pm q = \beta_{n\pm1}$, the right side of Eq. (24) is

$$\frac{\partial^2}{\partial t^2}\left(\frac{1}{2}\left(e^{i[\Omega t - qz + \phi]} + e^{-i[\Omega t - qz + \phi]}\right)\sum_n a_n(z)\psi_n(x,y)e^{i(\omega_n t - \beta_n z)}\right)$$
$$= -\frac{1}{2}\sum_n a_n(z)\psi_n(x,y)\left(\omega_{n+1}^2 e^{i(\omega_{n+1}t - \beta_{n+1}z)}e^{i\phi} + \omega_{n-1}^2 e^{i(\omega_{n-1}t - \beta_{n-1}z)}e^{-i\phi}\right), \quad (26)$$

By substituting $(n \pm 1)$ by n, we have

$$\sum_n a_n(z)\psi_n(x,y)\omega_{n\pm1}^2 e^{i(\omega_{n\pm1}t - \beta_{n\pm1}z)} = \sum_n a_{n\mp1}(z)\psi_{n\mp1}(x,y)\omega_n^2 e^{i(\omega_n t - \beta_n z)}, \quad (27)$$

since $\Omega \ll \omega_0$, the mode profiles satisfy $\psi_{n\pm1}(x, y) \approx \psi_n(x, y) \approx \psi_0(x, y)$, we can thus obtain the coupled-mode equation in the frequency dimension

$$i\frac{\partial a_n(z)}{\partial z} = J_\omega\left(e^{i\phi}a_{n-1}(z) + e^{-i\phi}a_{n+1}(z)\right), \quad (28)$$

where the frequency-dimension coupling strength is given by

$$J_\omega = \frac{\Delta\varepsilon \cdot \omega_n^2}{4\beta_n c^2} = \frac{\Delta n \beta_0}{2 n_0},$$
(29)

The coupled-mode equation of Eq. (28) can be rewritten as the Hamiltonian

$$H = \sum_n J_\omega \left(e^{-i\phi} \hat{a}_n^\dagger \hat{a}_{n+1} + h.c. \right),$$
(30)

Since the waveguides of A and B have different coupling strengths $J_{\omega 1}$, $J_{\omega 2}$ and phases ϕ_1, ϕ_2, the Hamiltonian for the frequency-dimension couplings is

$$H = \sum_n \left(J_{\omega 1} e^{-i\phi_1} \hat{a}_n^\dagger \hat{a}_{n+1} + J_{\omega 2} e^{-i\phi_2} \hat{b}_n^\dagger \hat{b}_{n+1} + h.c. \right).$$
(31)

Combined with the in-plane couplings in the brick-wall array, the 3D synthetic lattice can thus be described by the Hamiltonian given by Eq. (2).

Funding

References

1. S.-Y. Xu, I. Belopolski, N. Alidoust, M. Neupane, G. Bian, C. Zhang, R. Sankar, G. Chang, Z. Yuan, C.-C. Lee, S.-M. Huang, H. Zheng, J. Ma, D. S. Sanchez, B. Wang, A. Bansil, F. Chou, P. P. Shibayev, H. Lin, S. Jia, and M. Z. Hasan, "Discovery of a Weyl fermion semimetal and topological Fermi arcs," Science **349**(6248), 613–617 (2015).
2. H. M. Weng, C. Fang, Z. Fang, B. A. Bernevig, and X. Dai, "Weyl Semimetal Phase in Noncentrosymmetric Transition-Metal Monophosphides," Phys. Rev. X **5**(1), 011029 (2015).
3. B. Q. Lv, H. M. Weng, B. B. Fu, X. P. Wang, H. Miao, J. Ma, P. Richard, X. C. Huang, L. X. Zhao, G. F. Chen, Z. Fang, X. Dai, T. Qian, and H. Ding, "Experimental Discovery of Weyl Semimetal TaAs," Phys. Rev. X **5**(3), 031013 (2015).
4. B. Q. Lv, N. Xu, H. M. Weng, J. Z. Ma, P. Richard, X. C. Huang, L. X. Zhao, G. F. Chen, C. E. Matt, F. Bisti, V. N. Strocov, J. Mesot, Z. Fang, X. Dai, T. Qian, M. Shi, and H. Ding, "Observation of Weyl nodes in TaAs," Nat. Phys. **11**(9), 724–727 (2015).
5. X. Huang, L. Zhao, Y. Long, P. Wang, D. Chen, Z. Yang, H. Liang, M. Xue, H. Weng, Z. Fang, X. Dai, and G. Chen, "Observation of the Chiral-Anomaly-Induced Negative Magnetoresistance in 3D Weyl Semimetal TaAs," Phys. Rev. X **5**(3), 031023 (2015).
6. N. P. Armitage, E. J. Mele, and A. Vishwanath, "Weyl and Dirac semimetals in three-dimensional solids," Rev. Mod. Phys. **90**(1), 015001 (2018).
7. A. A. Soluyanov, D. Gresch, Z. Wang, Q. Wu, M. Troyer, X. Dai, and B. A. Bernevig, "Type-II Weyl semimetals," Nature **527**(7579), 495–498 (2015).
8. M. Trescher, B. Sbierski, P. W. Brouwer, and E. J. Bergholtz, "Quantum transport in Dirac materials: Signatures of tilted and anisotropic Dirac and Weyl cones," Phys. Rev. B **91**(11), 115135 (2015).
9. H. Zheng, G. Bian, G. Chang, H. Lu, S. Y. Xu, G. Wang, T. R. Chang, S. Zhang, I. Belopolski, N. Alidoust, D. S. Sanchez, F. Song, H. T. Jeng, N. Yao, A. Bansil, S. Jia, H. Lin, and M. Z. Hasan, "Atomic-Scale Visualization of Quasiparticle Interference on a Type-II Weyl Semimetal Surface," Phys. Rev. Lett. **117**(26), 266804 (2016).
10. M. N. Ali, J. Xiong, S. Flynn, J. Tao, Q. D. Gibson, L. M. Schoop, T. Liang, N. Haldolaarachchige, M. Hirschberger, N. P. Ong, and R. J. Cava, "Large, non-saturating magnetoresistance in WTe2," Nature **514**(7521), 205–208 (2014).
11. S. Tchoumakov, M. Civelli, and M. O. Goerbig, "Magnetic-Field-Induced Relativistic Properties in Type-I and Type-II Weyl Semimetals," Phys. Rev. Lett. **117**(8), 086402 (2016).
12. M. Udagawa and E. J. Bergholtz, "Field-Selective Anomaly and Chiral Mode Reversal in Type-II Weyl Materials," Phys. Rev. Lett. **117**(8), 086401 (2016).
13. L. Lu, L. Fu, J. D. Joannopoulos, and M. Soljačić, "Weyl points and line nodes in gyroid photonic crystals," Nat. Photonics **7**(4), 294–299 (2013).
14. L. Lu, Z. Wang, D. Ye, L. Ran, L. Fu, J. D. Joannopoulos, and M. Soljačić, "Experimental observation of Weyl points," Science **349**(6248), 622–624 (2015).
15. M. Xiao, Q. Lin, and S. Fan, "Hyperbolic Weyl Point in Reciprocal Chiral Metamaterials," Phys. Rev. Lett. **117**(5), 057401 (2016).

16. J. Noh, S. Huang, D. Leykam, Y. D. Chong, K. P. Chen, and M. C. Rechtsman, "Experimental observation of optical Weyl points and Fermi arc-like surface states," Nat. Phys. **13**(6), 611–617 (2017).

17. B. Yang, Q. Guo, B. Tremain, L. E. Barr, W. Gao, H. Liu, B. Béri, Y. Xiang, D. Fan, A. P. Hibbins, and S. Zhang, "Direct observation of topological surface-state arcs in photonic metamaterials," Nat. Commun. **8**(1), 97 (2017).

18. B. Yang, Q. Guo, B. Tremain, R. Liu, L. E. Barr, Q. Yan, W. Gao, H. Liu, Y. Xiang, J. Chen, C. Fang, A. Hibbins, L. Lu, and S. Zhang, "Ideal Weyl points and helicoid surface states in artificial photonic crystal structures," Science **359**(6379), 1013–1016 (2018).

19. M. Xiao, W.-J. Chen, W.-Y. He, and C. T. Chan, "Synthetic gauge flux and Weyl points in acoustic systems," Nat. Phys. **11**(11), 920–924 (2015).

20. Z. Yang and B. Zhang, "Acoustic Type-II Weyl Nodes from Stacking Dimerized Chains," Phys. Rev. Lett. **117**(22), 224301 (2016).

21. F. Li, X. Huang, J. Lu, J. Ma, and Z. Liu, "Weyl points and Fermi arcs in a chiral phononic crystal," Nat. Phys. **14**(1), 30–34 (2017).

22. G. G. Pyrialakos, N. S. Nye, N. V. Kantartzis, and D. N. Christodoulides, "Emergence of Type-II Dirac Points in Graphynelike Photonic Lattices," Phys. Rev. Lett. **119**(11), 113901 (2017).

23. Y. Sun, S.-C. Wu, M. N. Ali, C. Felser, and B. Yan, "Prediction of Weyl semimetal in orthorhombicMoTe2," Phys. Rev. B **92**(16), 161107 (2015).

24. Q. Lin, M. Xiao, L. Yuan, and S. Fan, "Photonic Weyl point in a two-dimensional resonator lattice with a synthetic frequency dimension," Nat. Commun. **7**, 13731 (2016).

25. Y. Zhang and Y. Zhu, "Generation of Weyl points in coupled optical microdisk-resonator arrays via external modulation," Phys. Rev. A **96**(1), 013811 (2017).

26. Q. Wang, M. Xiao, H. Liu, S. Zhu, and C. T. Chan, "Optical Interface States Protected by Synthetic Weyl Points," Phys. Rev. X **7**(3), 031032 (2017).

27. X. Y. Feng, G. M. Zhang, and T. Xiang, "Topological characterization of quantum phase transitions in a spin-1/2 model," Phys. Rev. Lett. **98**(8), 087204 (2007).

28. J. M. Hou and W. Chen, "Hidden symmetry and protection of Dirac points on the honeycomb lattice," Sci. Rep. **5**(1), 17571 (2015).

29. N. Goldman, G. Jotzu, M. Messer, F. Görg, R. Desbuquois, and T. Esslinger, "Creating topological interfaces and detecting chiral edge modes in a two-dimensional optical lattice," Phys. Rev. A **94**(4), 043611 (2016).

30. B. Dóra and R. Moessner, "Gauge field entanglement in Kitaev's honeycomb model," Phys. Rev. B **97**(3), 035109 (2018).

31. L. Yuan, Y. Shi, and S. Fan, "Photonic gauge potential in a system with a synthetic frequency dimension," Opt. Lett. **41**(4), 741–744 (2016).

32. L. Yuan and S. Fan, "Bloch oscillation and unidirectional translation of frequency in a dynamically modulated ring resonator," Optica **3**(9), 1014–1018 (2016).

33. C. Qin, F. Zhou, Y. Peng, D. Sounas, X. Zhu, B. Wang, J. Dong, X. Zhang, A. Alù, and P. Lu, "Spectrum Control through Discrete Frequency Diffraction in the Presence of Photonic Gauge Potentials," Phys. Rev. Lett. **120**(13), 133901 (2018).

34. C. Qin, L. Yuan, B. Wang, S. Fan, and P. Lu, "Effective electric-field force for a photon in a synthetic frequency lattice created in a waveguide modulator," Phys. Rev. A **97**(6), 063838 (2018).

35. C. Qin, B. Wang, H. Long, K. Wang, and P. Lu, "Nonreciprocal phase shift and mode modulation in dynamic graphene waveguides," J. Lightwave Technol. **34**(16), 3877–3883 (2016).

36. S. Ke, D. Zhao, Q. Liu, S. Wu, B. Wang, and P. Lu, "Optical Imaginary Directional Couplers," J. Lightwave Technol. **36**(12), 2510–2516 (2018).

37. S. Wang, C. Qin, B. Wang, and P. Lu, "Discrete temporal Talbot effect in synthetic mesh lattices," Opt. Express **26**(15), 19235 (2018).

38. P. B. Johnson and R. W. Christy, "Optical Constants of the Noble Metals," Phys. Rev. B **6**(12), 4370–4379 (1972).

39. S. A. Maier, Plasmonics: Fundamentals and Applications (Springer Verlag, 2007).

40. N. Liu, L. Langguth, T. Weiss, J. Kästel, M. Fleischhauer, T. Pfau, and H. Giessen, "Plasmonic analogue of electromagnetically induced transparency at the Drude damping limit," Nat. Mater. **8**(9), 758–762 (2009).

41. F. Wang, S. Ke, C. Qin, B. Wang, H. Long, K. Wang, and P. Lu, "Topological interface modes in graphene multilayer arrays," Opt. Laser Technol. **103**, 272–278 (2018).

42. L. D. Tzuang, K. Fang, P. Nussenzveig, S. Fan, and M. Lipson, "Non-reciprocal phase shift induced by an effective magnetic flux for light," Nat. Photonics **8**(9), 701–705 (2014).

43. H. V. Pham, H. Murata, and Y. Okamura, "Electrooptic Modulators with Controlled Frequency Responses by Using Nonperiodically Polarization-Reversed Structure," Adv. Optoelectron. **2008**, 1–8 (2008).

44. B. A. Bell, K. Wang, A. S. Solntsev, D. N. Neshev, A. A. Sukhorukov, and B. J. Eggleton, "Spectral photonic lattices with complex long-range coupling," Optica **4**(11), 1433 (2017).